

Inverse Design of Ultra-Compact and Low-Loss Optical Phase Shifters

Junpeng Liao ¹, Ye Tian ^{1,*}, Zhe Kang ² and Xiaowei Zhang ¹

¹ Department of Electrical Engineering and Computer Science, Ningbo University, Ningbo 315211, China; 2111082290@nbu.edu.cn (J.L.); zhangxiaowei@nbu.edu.cn (X.Z.)

² Centre for Optical and Electromagnetic Research, College of Optical Science and Engineering, Ningbo Innovation Center, Zhejiang University, Hangzhou 310058, China; zhe_kang@zju.edu.cn

* Correspondence: tianye@nbu.edu.cn

Abstract: In previous works, inverse design methods have primarily focused on manipulating the optical power to achieve specific design targets. In this paper, we use the inverse design method to enable the precise engineering of the optical phase. As a proof of concept, we present a series of phase shifters (PSs) with varying phase shifts, which are inversely designed and theoretically validated on the silicon-on-insulator (SOI) platform. The designed PSs exhibit remarkable accuracy, with deviations of below 1° . These proposed PSs feature an ultra-compact footprint of $3\ \mu\text{m}$ in length and offer superior fabrication tolerances compared to conventional structures. Over the 1535–1565 nm bandwidth, the discrepancy between the actual and target phase shifts remains below $\pm 1^\circ$ for all phase shifters, while the insertion loss is consistently below 0.035 dB. Moreover, the feasibility of the designed five PSs is verified using 2×2 multimode interference couplers (MMI).

Keywords: silicon photonics; silicon passive devices; inverse design



Citation: Liao, J.; Tian, Y.; Kang, Z.; Zhang, X. Inverse Design of Ultra-Compact and Low-Loss Optical Phase Shifters. *Photonics* **2023**, *10*, 1030. <https://doi.org/10.3390/photonics10091030>

Received: 19 July 2023

Revised: 6 September 2023

Accepted: 7 September 2023

Published: 8 September 2023



Copyright: © 2023 by the authors. Licensee MDPI, Basel, Switzerland. This article is an open access article distributed under the terms and conditions of the Creative Commons Attribution (CC BY) license (<https://creativecommons.org/licenses/by/4.0/>).

1. Introduction

Photonic Integrated Circuits (PICs) based on the Silicon-on-Insulator (SOI) platform have attracted much attention due to their high integration density and compatibility with CMOS processes [1–3]. Among the various integrated optical devices on the SOI platform, optical phase shifters (PSs) can be used not only for sensors [4], telecom and datacom applications [5,6], but also for quantum computing [7,8]. Of the reported PSs, there are two main types of structure, active and passive, which produce phase shifts by adjusting the corresponding optical path lengths or changing the propagation constants of the waveguide modes. Active PSs mainly use the thermo-optical effect of silicon photonic waveguides to modify the effective refractive index of the waveguide by means of on-chip metal microheaters to achieve a corresponding phase shift [9,10]. In contrast, passive PSs have no requirement for control elements or driving power, eliminating the constraint of power consumption and enabling applications in novel optical 90° hybrids [11], arbitrary ratio power splitters [12,13], and mode-division multiplexing (MDM) systems [14,15].

To date, only a few studies have been reported on passive PSs on SOI and the primary design approach is to induce a phase shift by controlling the waveguide length or width. Chaen et al. achieved a phase shift of 180° between two similar waveguides by simply increasing the length of one waveguide relative to another waveguide [16]. By changing the width of one waveguide, a phase shift of 90° or 180° between the two waveguides can be achieved, enabling butterfly-shaped PSs that can be used for TE_0 to TE_1 [17], TE_0 to TE_2 mode conversion [18] and demultiplexing of TE_0 and TE_1 modes [19]. Morrissey et al. implemented a PS with a phase shift of 180° by optimizing the width of a 1×1 multimode interference (MMI) coupler [20]. Moreover, using anisotropy and dispersion engineering in subwavelength metamaterial waveguides, a 90° PS with an ultra-broadband of 400 nm was realized by varying the longitudinal width of the subwavelength grating (SWG) [21].

However, the phase shift of the PS for these designs is typically 90° or 180° to apply to the higher-order modes required for processing in MDM systems. There is little research on PSs for special phase shifts such as 30°, 60°, etc. The flexibility of PICs can be effectively improved if PSs with arbitrary phase shifts can be implemented.

More recently, inverse design methods for photonic devices have been extensively reported, which can implement high-performance devices at a much smaller size [22–24]. However, most of the inverse design methods concentrate on the design of the mode power distribution in the waveguide, while very little inverse design research has been carried out for phase design. In this paper, we inversely design the passive PSs based on shape optimization. By optimizing the multi-segment width of the PS using particle swarm optimization (PSO), arbitrary phase shifts can be achieved. This paper validates a series of PSs with phase shifts of 1°, 30°, 60°, 90°, and 180°, respectively. The length of each PS is only 3 μm. Simulations show that the maximum phase shift error (PSE) for five PSs is below ±1° over the wavelength range 1535 to 1565 nm and all PSs exhibit extremely low insertion loss (IL) (<0.035 dB). In addition, the designed PSs are verified using 2 × 2 MMI. The verification results match with the simulation calculation results and prove the feasibility of the designed PSs. To the best of our knowledge, the proposed 90° and 180° PSs exhibit the smallest size and lowest losses.

2. Design Principle

Figure 1a depicts the schematic diagram of the proposed PS, which is designed on an SOI platform with a 220 nm core silicon layer and oxide cladding. The phase shift is achieved by varying the shape of the waveguide in the phase shift section (indicated by the dashed box). A straight waveguide with the same length is used as a reference to determine the resulting accumulated phase shift, denoted as ΔΦ. All designed PSs have a fixed length L of 3 μm and are connected to an input/output waveguide with a width W of 0.5 μm. The shape optimization principle for the PS is illustrated in Figure 1b. The shape of the PS is defined using three different widths (W₁, W₂, and W₃) equally distributed along the x-axis. For easier fabrication, the PS has a smooth and continuous boundary constructed by the cubic spline interpolation method. By optimizing the values of W₁, W₂, and W₃, the shape of PS can be adjusted to achieve the desired phase shift.

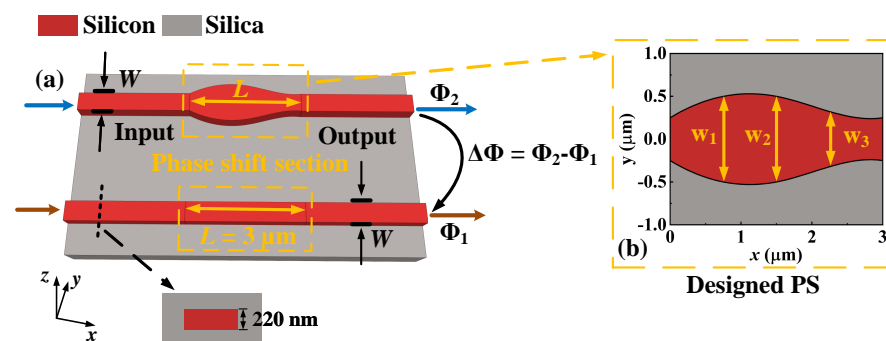


Figure 1. (a) The schematic diagram of the proposed PS. (b) The schematic diagram of the shape optimization principle for the PS.

Here, we use the PSO algorithm to optimize the three parameters. The PSO is a population-based stochastic optimization technique inspired by the social behavior of flocks of birds or schools of fish, which has been widely used to solve multi-parameter optimization problems due to its fast convergence [25,26]. The three-dimensional finite-difference time-domain (3D FDTD) method is used for the simulation of PS, phase calculation, and optimization objective calculation. The optimization objective is quantified by a figure of merit (FOM) and is expressed by the following equation:

$$FOM = \sum (|(\Delta\Phi_i - \Delta\Phi_i^*) \frac{\pi}{180}| + |T_i - 1|) \tag{1}$$

where $\Delta\Phi_i$ and $\Delta\Phi_i^*$ are the actual and target phase shifts at the i -th wavelength channel within the wavelength range of 1535–1565 nm. T_i is the normalized transmittance of the input TE₀ mode at the i -th wavelength channel. Most of the phase shifters are designed by considering only the device parameters as a function of phase shift and ignoring the possible variations in insertion loss. In Equation (1), we design the combination of phase shift and normalized transmittance of the device as FOM. The FOM is minimized by PSO, i.e., the FOM converges to 0. In this way, $\Delta\Phi$ converges to the target value $\Delta\Phi^*$ and T converges to 1, which ensures that the designed PS achieves the required phase shift with minimum losses. Considering the numerical balance between the two parts in Equation (1), the units of phase shift are converted from degree to radian to facilitate the calculation.

The detailed flow of optimizing W_1 , W_2 , and W_3 for phase design using the PSO algorithm is shown in Figure 2. The positions of the particles represent the values of W_1 , W_2 , and W_3 , while the velocities of the particles correspond to the variation range for these parameters. The positions and velocities of the particles are updated iteratively based on the following Equation [27]:

$$v_n = \omega v_{n-1} + r_1 \eta_1 (p_{\text{best},n-1} - z_{n-1}) + r_2 \eta_2 (g_{\text{best},n-1} - z_{n-1}) \tag{2}$$

$$z_n = z_{n-1} + v_n \tag{3}$$

where z and v represent the position and velocity of the particle, respectively. n denotes the iteration. p_{best} represents the best position achieved by the particle so far, and g_{best} represents the best position achieved by any particle in the entire swarm. The coefficients ω , r_1 , and r_2 control the impact of the previous velocity, the particle’s personal best, and the swarm’s global best on the update. η_1 and η_2 are random coefficients between 0 and 1. To ensure better search results, a wide range of parameters is considered for optimization, where W_1 , W_2 , and $W_3 \in [0.2 \mu\text{m}, 0.8 \mu\text{m}]$. At each iteration, the FOM obtained from the 3D FDTD is used as an evaluation metric to find the appropriate p_{best} and g_{best} to minimize the FOM. Afterward, the position and velocity of the particles are updated according to Equations (2) and (3), and the optimization is stopped to obtain the final result when the set number of iterations is reached.

A common approach to designing phase shifters usually starts with parameters such as the length or overall width of the device. By scanning these basic parameters of the device, it is possible to obtain them as a function of phase shift. However, this approach may face the problem of unconstrained device dimensions and the fact that the phase shift of a device is relatively sensitive to variations in its parameters. In contrast, the inverse design method in this paper starts with the target phase shift and allows the device shape to be designed for arbitrary phase shifts by optimizing the multi-segment width of the device in an ultra-compact footprint of $3 \mu\text{m} \times 0.8 \mu\text{m}$. As a result, the designed devices are smaller in size and robust to fabrication errors. We validated the design of five PSs with different phase shifts by setting $\Delta\Phi^* = 1^\circ, 30^\circ, 60^\circ, 90^\circ$, and 180° . After 80 iterations of PSO, the W_1 , W_2 , and W_3 values corresponding to each PS of the design are listed in Table 1. The final structures with smooth boundaries are shown in Figure 3. All PSs have a length of $3 \mu\text{m}$ and a width between $0.3 \mu\text{m}$ and $0.8 \mu\text{m}$. The inset of Figure 3 shows the electric field distribution at 1550 nm for the corresponding PSs and it can be clearly observed that the light propagates directly along the PSs with negligible loss.

Table 1. Optimization results for parameters W_1 , W_2 and W_3 .

Parameters	1° PS	30° PS	60° PS	90° PS	180° PS
W_1 (μm)	0.389	0.513	0.799	0.8	0.386
W_2 (μm)	0.534	0.632	0.659	0.789	0.342
W_3 (μm)	0.712	0.538	0.45	0.522	0.377

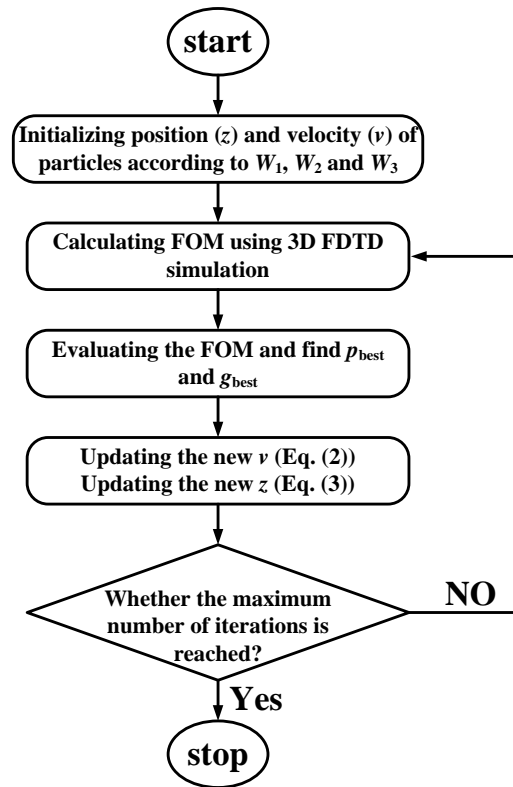


Figure 2. The flow chart of PSO algorithm.

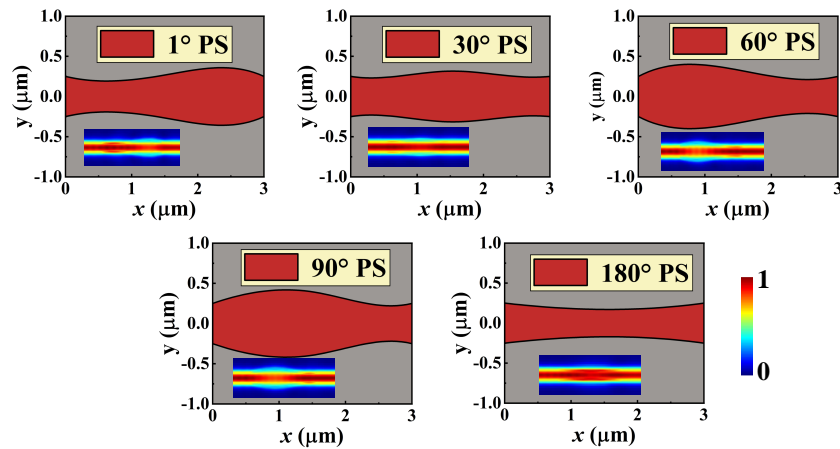


Figure 3. Schematic diagram of the structure of the designed PSs with varying phase shifts. Inset: Electric field distribution at 1550 nm for the corresponding PS.

3. Results and Discussion

The performance of the PSs is evaluated by examining two key metrics: the phase shift error (PSE) and the insertion loss (IL). The PSE is defined as the deviation between the achieved phase shift and the target phase shift, which can be written as:

$$PSE = \Delta\Phi - \Delta\Phi^* \tag{4}$$

and the IL can be written as:

$$IL = -10\log_{10}(T_{\text{output}}) \tag{5}$$

where T_{output} is the transmittance at the output port of the PS. The calculated phase shifts and corresponding PSEs for the five PSs are shown in Figure 4a–e. At 1550 nm, the achieved

phase shifts for these PSs are 1° , 30.01° , 60.02° , 89.99° , and 180° , respectively. Consequently, the PSEs of the five PSs at 1550 nm are as slight as 0° , 0.01° , 0.02° , -0.01° and 0° , respectively. Within the wavelength range of 1535–1565 nm, the achieved phase shifts of the five PSs vary from 1.07° to 0.94° , 29.85° to 30.16° , 59.66° to 60.38° , 89.25° to 90.37° and 180.88° to 179.21° , respectively. Accordingly, in the PSEs of the five PSs in this 30 nm wavelength, the ranges are below $\pm 0.07^\circ$, $\pm 0.16^\circ$, $\pm 0.38^\circ$, $\pm 0.75^\circ$, and $\pm 0.88^\circ$, respectively. It is evident that the designed PSs exhibit minimal phase shift errors, and the maximum PSE among the five PSs at the central wavelength is only 0.02° . Furthermore, across the entire bandwidth of 1535–1565 nm, all PSs maintain a PSE below $\pm 1^\circ$. The successful implementation of the 1° PS also demonstrates the accuracy achievable with the proposed design method, as it closely matches the desired phase shift. In addition, the calculated IL curves for the five PSs are shown in Figure 4f. It can be seen that the designed PSs all exhibit extremely low IL, with each PS having an IL of less than 0.032 dB within the wavelength range from 1535 to 1565 nm.

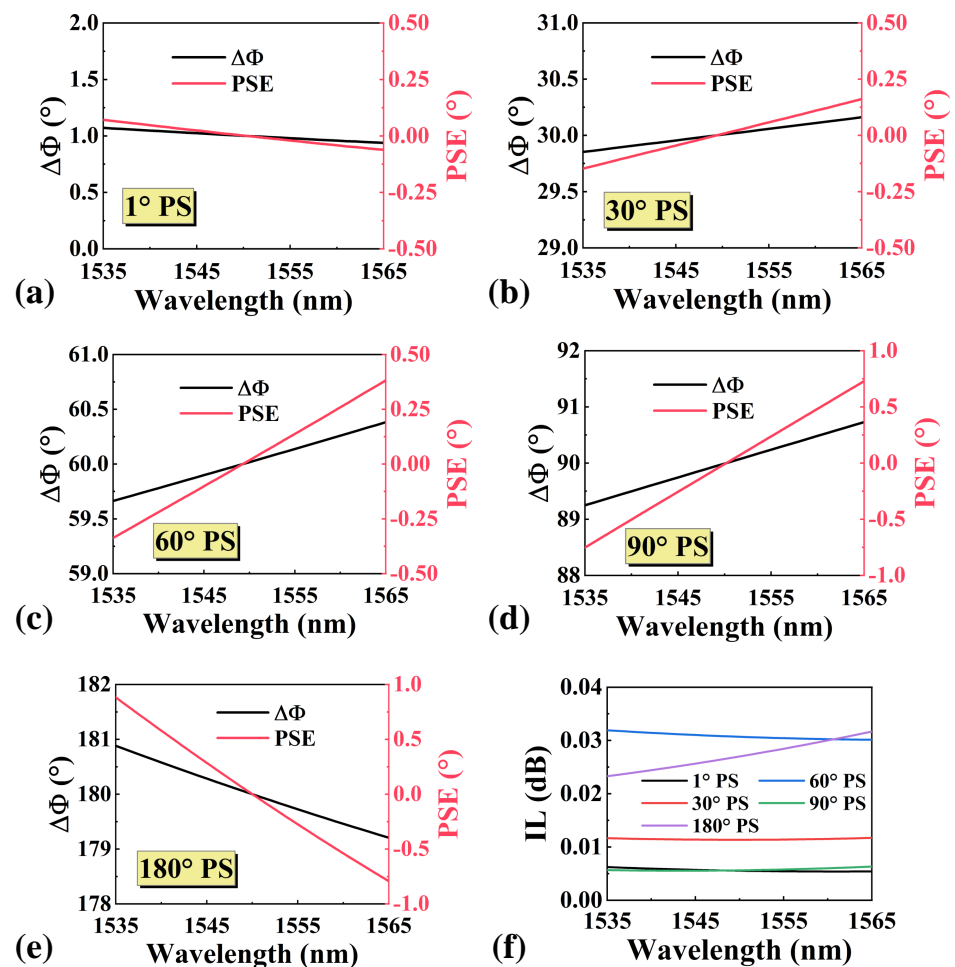


Figure 4. Calculated phase shift and PSE for (a) 1° PS, (b) 30° PS, (c) 60° PS, (d) 90° PS, and (e) 180° PS. (f) Calculated IL curves for the designed PSs.

The tolerance to fabrication errors of the five PSs is investigated by varying the waveguide width (ΔW) within a range of -20 nm to 20 nm, as illustrated in Figure 5a. The maximum absolute value of PSE at each wavelength is calculated for each wavelength within the range of 1535 nm to 1565 nm and is shown in Figure 5b. It is observed that the maximum absolute value of PSE for all PSs in the 30 nm wavelength range is 7.6° . In comparison, the maximum absolute value of PSE reaches 10° with the same variation for both the conventional butterfly PS and the MMI-based PS [20,21]. Figure 5c presents the maximum variation in IL due to the width changes for all PSs within the wavelength range

of 1535 nm to 1565 nm. It can be observed that the IL is minimally affected by the width variation, with the maximum IL remaining below 0.035 dB in the entire 30 nm wavelength range. This demonstrates that our designed PSs exhibit favorable fabrication tolerances, as the IL remains consistently low even with variations in the waveguide width.

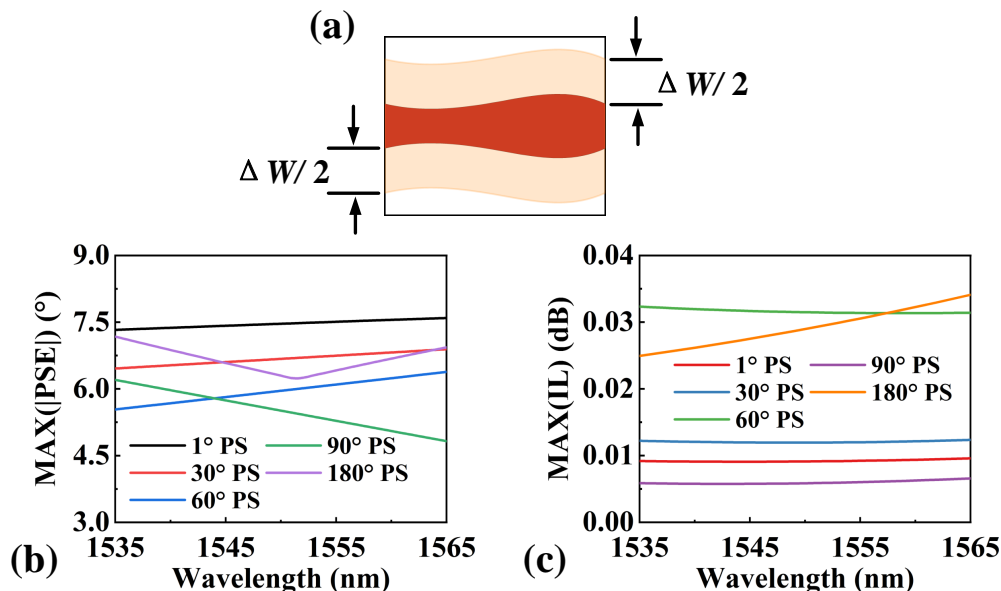


Figure 5. As ΔW varies from -20 nm to 20 nm, (a) the schematic of the variation in the width of the designed PS, (b) the maximum absolute value of PSE, and (c) maximum IL within the wavelength range of 1535 to 1565 nm.

To validate the feasibility of the designed PSs, the characterization setup of 2×2 MMI was used to further the simulation verification of the PSs, as depicted in Figure 6a. In this validation structure, TE_0 lights with equal power are injected at input port 1 and input port 2. Then, the PS on the lower arm introduces the corresponding phase shift to the transmitted light. Finally, the two TE_0 lights with phase difference $\Delta\Phi'$ are coupled into the 2×2 MMI. The dimensions for 2×2 MMI are adopted from Guan et al. [28]. Figure 6b–f illustrate the electric field distribution at 1550 nm for the validation structures of five PSs. It is evident that the power distribution at output port 1 and port 2 varies for different phase shifters. The transmission spectra of employed 2×2 MMI as a function of phase difference $\Delta\Phi'$ are shown in Figure 6g. By analyzing the output power distribution, we can determine the phase shift induced by the PSs. The power distribution at the outputs for all validation structures is also marked in the figure, with circles indicating the power from the out port 1 and forks indicating the power from the out port 2. The phase shifts for the proposed PSs at 1550 nm are estimated as 1.04° , 29.96° , 59.94° , 89.91° , and 179.98° , respectively. Consequently, the corresponding PSEs are 0.04° , -0.04° , -0.06° , -0.09° , and -0.02° , respectively. The phase shifts of all PSs are also verified within the wavelength range from 1535 to 1565 nm, and the calculated PSE curves are shown in Figure 6h. It can be observed that the PSEs for 1° PS, 30° PS, 60° PS, 90° PS and 180° PS are below $\pm 0.16^\circ$, $\pm 0.3^\circ$, $\pm 0.63^\circ$, $\pm 0.52^\circ$ and $\pm 0.99^\circ$ over the 30 nm bandwidth, respectively. Compared to the theoretical analysis, There is a slight mismatch ($\leq \pm 0.25^\circ$) with the results obtained from 2×2 MMI structures. The slight discrepancy may be attributed to differences in the overall simulation area, leading to variations in the grid accuracy for the 3D FDTD simulations employed in the characterization setup.

Additionally, Table 2 provides a comparison between our work and previously reported passive optical PSs. It is evident that the PSs designed in this paper exhibit significant advantages in terms of footprint and losses, representing the smallest passive PSs reported to date.

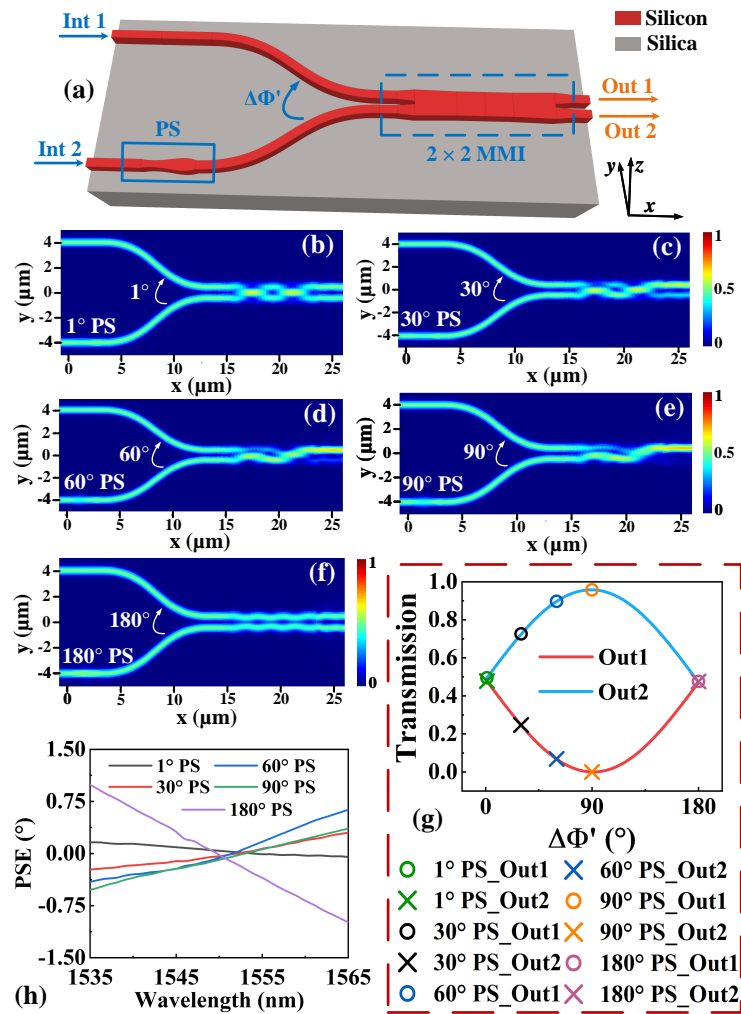


Figure 6. (a) The Schematic diagram of the test structure used to characterize the PSs. The electric field distribution of the tested structures at 1550 nm for (b) 1° PS, (c) 30° PS, (d) 60° PS, (e) 90° PS, and (f) 180° PS. (g) Transmission spectra of 2 × 2 MMI at 1550 nm when two signals with phase difference $\Delta\Phi'$ are input. Circles indicate power from test structure output port 1 and forks indicate power from test structure output port 2. (h) PSE curves for all PSs validated in the wavelength range of 1535 to 1565 nm.

Table 2. Comparison of Reported Phase shifters.

Reference	Length (μm)	Phase (°)	PSE (°)	IL (dB)	Bandwidth (nm)
[18]	156	180	-	<0.3	35
[19]	3.41	90	<±1	-	30
[20]	7	180	<±1	<0.25	30
[21]	16.8	90	<±0.8	<0.15	400
this work	3	90	<±0.8	<0.01	30
		180	<±0.9	<0.03	30

4. Conclusions

In conclusion, our study presents a novel PS with arbitrary phase shift designed using a shape optimization method. Five PSs with phase shifts of 1°, 30°, 60°, 90° and 180° are demonstrated. All five PSs are designed in an ultra-compact size of only 3 μm in length. Simulation results show that the maximum PSE for all PSs remains below ±1° over a wavelength range of 30 nm (1535–1565 nm) and the maximum IL for all phase shifters is only 0.035 dB. The designed PSs are verified using 2 × 2 MMI. The verification results

match the simulation results with an error of less than $\pm 0.25^\circ$ between the results. We believe that the arbitrary phase shift PS demonstrated in this paper could find potential applications in coherent communications, quantum photonics, and MDM circuits.

Author Contributions: Conceptualization, J.L. and Y.T.; methodology, J.L. and Y.T.; software, Z.K.; validation, Y.T. and Z.K.; formal analysis, X.Z.; investigation, J.L.; resources, Y.T.; data curation, X.Z.; writing—original draft preparation, J.L.; writing—review and editing, Y.T.; visualization, Z.K.; supervision, X.Z.; project administration, Y.T.; funding acquisition, Y.T. All authors have read and agreed to the published version of the manuscript.

Funding: This work was supported by the National Natural Science Foundation of China (62105167, 62075188, 61974078), the Natural Science Foundation of Zhejiang Province (LQ22F050008, LY21F050007), the Natural Science Foundation of Ningbo (2021J074, 2021J059), and the Key Research and Development Program of Jiangsu Province (BE2021082).

Institutional Review Board Statement: Not applicable.

Informed Consent Statement: Not applicable.

Data Availability Statement: The data that support the findings of this study are available from the corresponding author upon reasonable request.

Acknowledgments: The authors express their appreciation to the anonymous reviewers for their valuable suggestions.

Conflicts of Interest: The authors declare no conflict of interest.

References

1. Lin, Z.; Rusch, L.; Chen, Y.; Shi, W. Chip-scale, full-Stokes polarimeter. *Opt. Express* **2019**, *27*, 4867–4877. [[CrossRef](#)] [[PubMed](#)]
2. Dong, P.; Chen, Y.K.; Duan, G.H.; Neilson, D.T. Silicon photonic devices and integrated circuits. *Nanophotonics* **2014**, *3*, 215–228. [[CrossRef](#)]
3. Hochberg, M.; Baehr-Jones, T. Towards fabless silicon photonics. *Nat. Photonics* **2010**, *4*, 492–494. [[CrossRef](#)]
4. Wu, W.J.; Zhao, W.S. A Quality Factor Enhanced Microwave Sensor Based on Modified Split-Ring Resonator for Microfluidic Applications. *IEEE Sens. J.* **2022**, *22*, 22582–22590. [[CrossRef](#)]
5. Hillerkuss, D.; Winter, M.; Teschke, M.; Marculescu, A.; Li, J.; Sigurdsson, G.; Worms, K.; Ezra, S.B.; Narkiss, N.; Freude, W.; et al. Simple all-optical FFT scheme enabling Tbit/s real-time signal processing. *Opt. Express* **2010**, *18*, 9324–9340. [[CrossRef](#)]
6. Doerr, C.R.; Winzer, P.J.; Chen, Y.K.; Chandrasekhar, S.; Rasras, M.S.; Chen, L.; Liow, T.Y.; Ang, K.W.; Lo, G.Q. Monolithic polarization and phase diversity coherent receiver in silicon. *J. Light. Technol.* **2009**, *28*, 520–525. [[CrossRef](#)]
7. Knill, E.; Laflamme, R.; Milburn, G.J. A scheme for efficient quantum computation with linear optics. *Nature* **2001**, *409*, 46–52. [[CrossRef](#)] [[PubMed](#)]
8. Harris, N.C.; Bunandar, D.; Pant, M.; Steinbrecher, G.R.; Mower, J.; Prabhu, M.; Baehr-Jones, T.; Hochberg, M.; Englund, D. Large-scale quantum photonic circuits in silicon. *Nanophotonics* **2016**, *5*, 456–468. [[CrossRef](#)]
9. Zhao, W.; Liu, R.; Peng, Y.; Yi, X.; Chen, H.; Dai, D. High-performance silicon polarization switch based on a Mach–Zehnder interferometer integrated with polarization-dependent mode converters. *Nanophotonics* **2022**, *11*, 2293–2301. [[CrossRef](#)]
10. Nikbakht, H.; Khoshmehr, M.T.; Van Someren, B.; Teichrib, D.; Hammer, M.; Förstner, J.; Akca, B.I. Asymmetric, non-uniform 3-dB directional coupler with 300-nm bandwidth and a small footprint. *Opt. Lett.* **2023**, *48*, 207–210. [[CrossRef](#)]
11. Jeong, S.H.; Morito, K. Novel Optical 90° Hybrid Consisting of a Paired Interference Based 2×4 MMI Coupler, a Phase Shifter and a 2×2 MMI Coupler. *J. Light. Technol.* **2010**, *28*, 1323–1331. [[CrossRef](#)]
12. Cherchi, M.; Ylino, S.; Harjanne, M.; Kapulainen, M.; Vehmas, T.; Aalto, T. Unconstrained splitting ratios in compact double-MMI couplers. *Opt. Express* **2014**, *22*, 9245–9253. [[CrossRef](#)] [[PubMed](#)]
13. Saida, T.; Himeno, A.; Okuno, M.; Sugita, A.; Okamoto, K. Silica-based 2×2 multimode interference coupler with arbitrary power splitting ratio. *Electron. Lett.* **1999**, *35*, 2031–2033. [[CrossRef](#)]
14. Priti, R.B.; Bazargani, H.P.; Xiong, Y.; Liboiron-Ladouceur, O. Mode selecting switch using multimode interference for on-chip optical interconnects. *Opt. Lett.* **2017**, *42*, 4131–4134. [[CrossRef](#)] [[PubMed](#)]
15. González-Andrade, D.; Olivares, I.; de Cabo, R.F.; Vilas, J.; Dias, A.; Velasco, A.V. Broadband three-mode converter and multiplexer based on cascaded symmetric Y-junctions and subwavelength engineered MMI and phase shifters. *Opt. Laser Technol.* **2023**, *164*, 109513. [[CrossRef](#)]
16. Chaen, Y.; Tanabe, K.; Jiang, H.; Hamamoto, K. Low wavelength dependency design for MMI (multi-mode interference) mode converter. *IEICE Electron. Express* **2015**, *12*, 20150727. [[CrossRef](#)]
17. Truong, C.D.; Nguyen, T.H.; Pham, Q.T.; Trinh, M.T.; Vu, K. Three-mode multiplexer and demultiplexer utilizing trident and multimode couplers. *Opt. Commun.* **2019**, *435*, 334–340. [[CrossRef](#)]

18. Qiu, J.; Zhang, D.; Tian, Y.; Wu, J.; Li, Y.; Wang, Y. Performance analysis of a broadband second-order mode converter based on multimode interference coupler and phase shifter. *IEEE Photonics J.* **2015**, *7*, 1–8.
19. González-Andrade, D.; Wangüemert-Pérez, J.G.; Velasco, A.V.; Ortega-Monux, A.; Herrero-Bermello, A.; Molina-Fernandez, I.; Halir, R.; Cheben, P. Ultra-broadband mode converter and multiplexer based on sub-wavelength structures. *IEEE Photonics J.* **2018**, *10*, 1–10. [[CrossRef](#)]
20. Morrissey, P.; Peters, F. Multimode interference couplers as compact and robust static optical phase shifters. *Opt. Commun.* **2015**, *345*, 1–5. [[CrossRef](#)]
21. González-Andrade, D.; Luque-González, J.M.; Wangüemert-Pérez, J.G.; Ortega-Monux, A.; Cheben, P.; Molina-Fernández, Í.; Velasco, A.V. Ultra-broadband nanophotonic phase shifter based on subwavelength metamaterial waveguides. *Photonics Res.* **2020**, *8*, 359–367. [[CrossRef](#)]
22. Molesky, S.; Lin, Z.; Piggott, A.Y.; Jin, W.; Vucković, J.; Rodriguez, A.W. Inverse design in nanophotonics. *Nat. Photonics* **2018**, *12*, 659–670. [[CrossRef](#)]
23. Zhang, G.; Xu, D.X.; Grinberg, Y.; Liboiron-Ladouceur, O. Experimental demonstration of robust nanophotonic devices optimized by topological inverse design with energy constraint. *Photonics Res.* **2022**, *10*, 1787–1802. [[CrossRef](#)]
24. Kim, J.; Kim, J.Y.; Yoon, J.; Yoon, H.; Park, H.H.; Kurt, H. Experimental demonstration of inverse-designed silicon integrated photonic power splitters. *Nanophotonics* **2022**, *11*, 4581–4590. [[CrossRef](#)]
25. Goudarzi, K.; Lee, M. Inverse design of a binary waveguide crossing by the particle swarm optimization algorithm. *Results Phys.* **2022**, *34*, 105268. [[CrossRef](#)]
26. Chen, W.; Li, H.; Zhang, B.; Wang, P.; Dai, S.; Liu, Y.; Li, J.; Li, Y.; Fu, Q.; Dai, T.; et al. Silicon mode (de) multiplexer based on cascaded particle-swarm-optimized counter-tapered couplers. *IEEE Photonics J.* **2020**, *13*, 1–10. [[CrossRef](#)]
27. Robinson, J.; Rahmat-Samii, Y. Particle swarm optimization in electromagnetics. *IEEE Trans. Antennas Propag.* **2004**, *52*, 397–407. [[CrossRef](#)]
28. Guan, H.; Ma, Y.; Shi, R.; Zhu, X.; Younce, R.; Chen, Y.; Roman, J.; Ophir, N.; Liu, Y.; Ding, R.; et al. Compact and low loss 90° optical hybrid on a silicon-on-insulator platform. *Opt. Express* **2017**, *25*, 28957–28968. [[CrossRef](#)]

Disclaimer/Publisher’s Note: The statements, opinions and data contained in all publications are solely those of the individual author(s) and contributor(s) and not of MDPI and/or the editor(s). MDPI and/or the editor(s) disclaim responsibility for any injury to people or property resulting from any ideas, methods, instructions or products referred to in the content.